Supplement of Atmos. Chem. Phys., 24, 9573–9595, 2024
https://doi.org/10.5194/acp-24-9573-2024-supplement

Atmospheric Chemistry and Physics
Open Access
EGU

Supplement of

Using observed urban NO_x sinks to constrain VOC reactivity and the ozone and radical budget in the Seoul Metropolitan Area

Benjamin A. Nault et al.

Correspondence to: Benjamin A. Nault (bnault@aerodyne.com, bnault1@jh.edu)

S1. Analytical Equation for $P(O_x)$

The analytical description of $P(O_x)$ and impacts from ΣANs chemistry has been described elsewhere (Farmer et al., 2011 and references therein). Briefly, $P(O_x)$ can be described by combining the following equations (Eq. S1 – S8). These equations are assumed to describe $P(O_x)$ for a single time during the day and is derived from the assumption that the HO_x radicals (HO_x = OH + HO_2 + RO_2) are in photostationary steady-state. The steady-state assumption for HO_x means production and loss are equal.

$$P(HO_x) = L(HO_x) = k_{OH+NO_2}[\mathrm{OH}][\mathrm{NO_2}] + \alpha k_{NO+RO_2}[\mathrm{NO}][\mathrm{RO_2}] + 2k_{HO_2+HO_2}[\mathrm{HO_2}][\mathrm{HO_2}] + 2k_{RO_2+HO_2}[\mathrm{HO_2}][\mathrm{RO_2}] + 2k_{RO_2+RO_2}[\mathrm{RO_2}][\mathrm{RO_2}] \quad \text{(Eq. S1)}$$

As described elsewhere, under the assumption of rapid $P(O_x)$ and thus radical chain propagation dominates, every RO_2 that is produced by the photooxidation of a VOC by OH will react with an NO molecule (R2, Sect. 1), and some fraction of the time (e.g., 1 – α, the effective branching ratio), produce HO_2 following the reaction of the alkoxy radical (RO) with O_2. Therefore, it is assumed that,

$$[\mathrm{HO_2}] \approx [\mathrm{RO_2}] \approx \frac{k_{OH+VOC}[\mathrm{VOC}][\mathrm{OH}]}{(1-\alpha)k_{NO+RO_2}[\mathrm{NO}]} \quad \text{(Eq. S2)}$$

Combining Eq. S1 and S2 together with an assumed, constant $P(HO_x)$, [OH] can be calculated using the quadratic formula:

$$[OH_{Calc}] = \frac{-b \pm \sqrt{b^2-4ac}}{2a} \quad \text{(Eq. S3)}$$

where

$$a = (2k_{HO_2+HO_2} + 2k_{RO_2+HO_2} + 2k_{RO_2+RO_2})\left(\frac{k_{OH+VOC}[\mathrm{VOC}]}{(1-\alpha)k_{NO+RO_2}[\mathrm{NO}]}\right)^2 \quad \text{(Eq. S4)}$$

$$b = k_{OH+NO_2}[\mathrm{NO_2}] + \frac{\alpha k_{NO+RO_2}}{(1-\alpha)k_{NO+RO_2}} \quad \text{(Eq. S5)}$$

$$c = -P(HO_x) \quad \text{(Eq. S6)}$$

In the above equations, k is the rate constant for the described reaction in the subtext (e.g., HO_2 + HO_2), the term k_{OH+VOC}[VOC] can be simplified to the VOC reactivity (R(VOC), s^{-1}) for the ambient mixture of VOCs, α is the effective branching ratio for the ambient mixture of VOCs, and $P(HO_x)$ is the HO_x production rate for the ambient mixture of gases. The rate constants for the two HO_x self-reactions, HO_2 ($k_{HO_2+HO_2}$) and RO_2 ($k_{RO_2+RO_2}$), and the HO_2-RO_2 reaction ($k_{HO_2+RO_2}$) were taken from Sander et al. (2011) for temperatures at 298 K and are 1.4×10^{-12}, 6.8×10^{-14}, and 8×10^{-12} cm^3 $molec.^{-1}$ s^{-1}, respectively. The OH and NO_2 rate constant is also from Sander et al. (2011) for temperatures at 298 K and is 1.2×10^{-11} cm^3 $molec.^{-1}$ s^{-1}. For the base case used here, $P(HO_x)$ is assumed to be 1×10^7 molec. cm^{-3} s^{-1}, α is 0, and R(VOC) (k_{OH+VOC}[VOC]) is 5.00 s^{-1}. Finally, the instantaneous $P(O_x)$ can be approximated as

$$P(O_x) = k_{HO_2+NO}[\mathrm{HO_2}][\mathrm{NO}] + (1-\alpha)k_{RO_2+NO}[\mathrm{RO_2}][\mathrm{NO}] \quad \text{(Eq. S7)}$$

$$P(O_x) = 2(1-\alpha)k_{OH+VOC}[\mathrm{VOC}][\mathrm{OH_{Calc}}] \quad \text{(Eq. S8)}$$

Note, that α controls both $P(O_x)$ (Eq. S8) and [OH_{Calc}] (Eq. S1, S2, S4, and S5). Thus, reducing α reduces both [OH_{Calc}] by ~40% (going from α = 0.1 to 0.05) and $P(O_x)$ by ~10%.

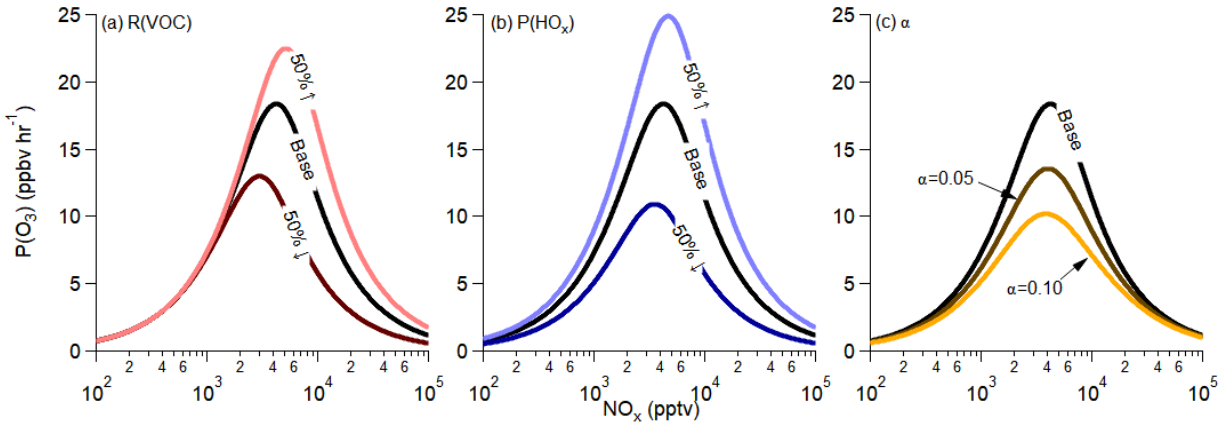

Figure S1. Example analytical solutions to instantaneous $P(O_x)$, assuming different scenarios with changes in total VOC reactivity (R(VOC)) (a), changes in HO_x radical production ($P(HO_x)$) (b), or changes in the alkyl and multi-functional nitrate effective branching ratio (α) (c). See Sect. S1 and Eq. S1 – S8 for the analytical equations. Note, for all scenarios/panels here, R(VOC), $P(HO_x)$, and α are constants, as discussed above and shown in Eq. S1 – S8.

Table S1. Measured VOCs and their associated MCMv3.3.1 species in F0AM.

MCMv3.3.1 species	Aircraft observation
CH3CHO	Acetaldehyde (PTRMS)
CH3COCH3	Acetone (PTRMS)
BENZENE	Benzene (PTRMS)
TOLUENE	Toluene (PTRMS)
MXYL	C8 alkylbenzenes (PTRMS)*20%[1,2]
PXYLE	C8 alkylbenzenes (PTRMS)*20%[1,2]
OXYLE	C8 alkylbenzenes (PTRMS)*17%[1]
STYRENE	C8 alkylbenzenes (PTRMS)*2%[1]
EBENZ	C8 alkylbenzenes (PTRMS)*41%[1]
C2H4	Ethene (WAS)
C2H2	Ethyne (WAS)
C2H6	Ethane (WAS)
C5H8	Isoprene (WAS)
IC4H10	i-Butane (WAS)
NC4H10	n-Butane (WAS)
IC5H12	i-Pentane (WAS)
NC5H12	n-Pentane (WAS)
PBENZ	i-Propylbenzene + n-Propylbenzene (WAS)
MEK	MEK (PTRMS)
CH3OH	Methanol (PTRMS)
C2H5OH	Methanol/2.5[3]
NC7H16	n-Heptane (WAS)
NC10H22	n-Decane (WAS)
NC6H14	n-Hexane (WAS)
NC8H18	n-Octane (WAS)
C3H8	Propane (WAS)
C3H6	Propene (WAS)
C4H6	1,3-Butadiene (WAS)
OETHTOL	2-Ethytoluene (WAS)
METHTOL	3-Ethyltoluene (WAS)
PETHTOL	4-Ethytoluene (WAS)
TM123B	1,2,3-Trimethylbenzene (WAS)
TM124B	1,2,4-Trimethylbenzene (WAS)
TM135B	1,3,5-Trimethylbenzene (WAS)
BPINENE	Monoterpenes (PTRMS)*0.45[1]
APINENE	Monoterpenes (PTRMS)*0.55[1]

[1]Speciated based on WAS measurements.
[2]Assume 50/50 split m-xylene vs. p-xylene.
[3]According to Schroeder et al. (2020)

Table S2. The higher PNs lumping based on their primary precursor species from F0AM.

Lumped PN	Primary Precursors	Largest PN in MCMv3.3.1
Arom	Aromatics: benzene, toluene, xylenes, ethylbenzene, propylbenzene, ethyltoluene, trimethylbenzenes, styrene	ACCOMEPAN
Alk	MEK, butane, pentane, decane, etc.	C3PAN1
Isop	Isoprene	CO2C3PAN
Monoterpenes	Monoterpenes	C3PAN2

S2. Comparison of NO_2 Measurements

There were three different measurements of NO_2 on the DC-8 during KORUS-AQ: (1) by chemiluminescence (Weinheimer et al., 1994), (2) by laser induced fluorescence (Thornton et al., 2000), and (3) by cavity enhanced absorption spectroscopy (Min et al., 2016). Here, only chemiluminescence and laser induced fluorescence are considered. Comparison of the NO_2 mixing ratios by these two measurements are shown in Figure S2. Though the correlation is high (R^2 = 1.00), the laser induced fluorescence NO_2 is ~16% higher than the chemiluminescence NO_2. To determine which NO_2 to use for the study, the NO_2-to-NO ratio was compared, as this ratio can be calculated with the observations on the DC-8. This ratio is defined by Eq. S9:

$$\frac{[NO_2]}{[NO]} = \frac{k_{NO+O_3}[O_3]+k_{NO+HO_2}[HO_2]+k_{NO+RO_2}[RO_2]}{j_{NO_2}} \quad \text{(Eq. S9)}$$

Note, though steady-state RO_2 is used throughout the paper and can provide some uncertainty in the calculated NO_2-to-NO ratio in Eq. S9, at high NO mixing ratios where both HO_2 and RO_2 concentrations are low, the O_3 + NO reaction dominates the term. It was found that the NO_2-to-NO ratio using the University of California, Berkeley, NO_2 generally agreed better with the calculated NO_2-to-NO ratio from Eq. S9. However, both NO_2-to-NO ratios 1σ spread of observations overlap with the calculated NO_2-to-NO ratio from Eq. S9. Thus, the University of California, Berkeley, NO_2 measurements are used throughout the manuscript. The use of the NCAR NO_2 had small changes but does not change the main conclusions and trends discussed throughout the paper.

Finally, photostationary steady-state (PSS) NO_2, calculated through rearrangement of Eq. S9, is compared against the measured NO_2 by chemiluminescence (CL) and laser induced fluorescence (LIF) in Fig. S4. The measured $NO_{2,LIF}$ versus $NO_{2,PSS}$ is closer to the one-to-one line (slope = 1.06) compared to the measured $NO_{2,CL}$ versus $NO_{2,PSS}$ (slope = 1.23). This further

supports the results in Fig. S3, showing that the $NO_{2,LIF}$ (NO_2 UCB in Fig. S3) is closer to the

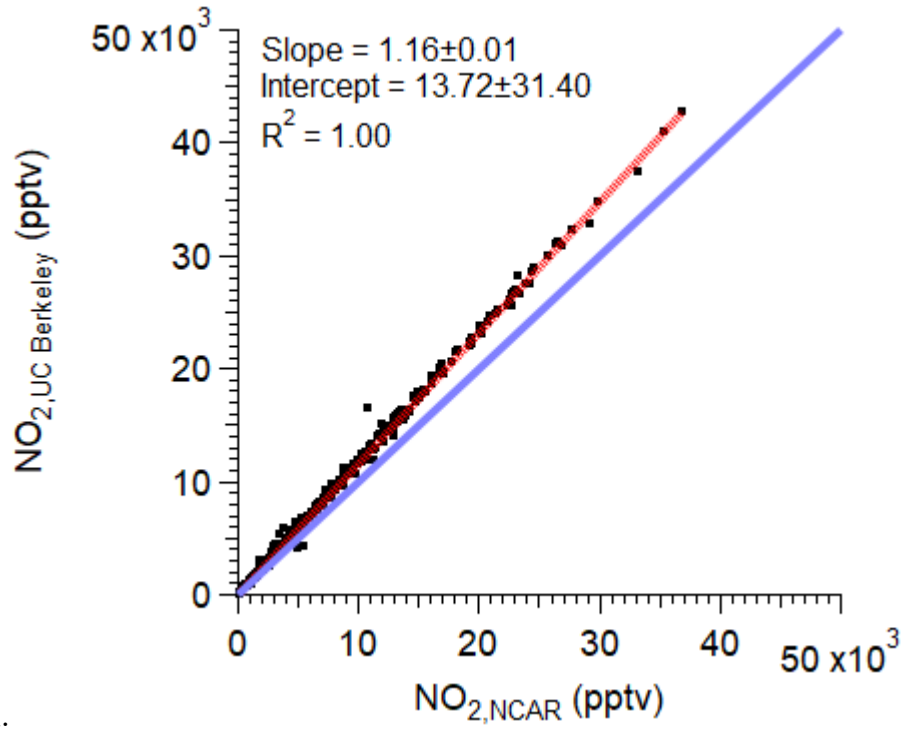

predicted PSS NO_2.

Figure S2. Scatter plot of the NO_2 measured by University of California, Berkeley, laser induced fluorescence and the NCAR chemiluminescence. The one-to-one line is shown in blue and the ODR fit for the data is shown in red.

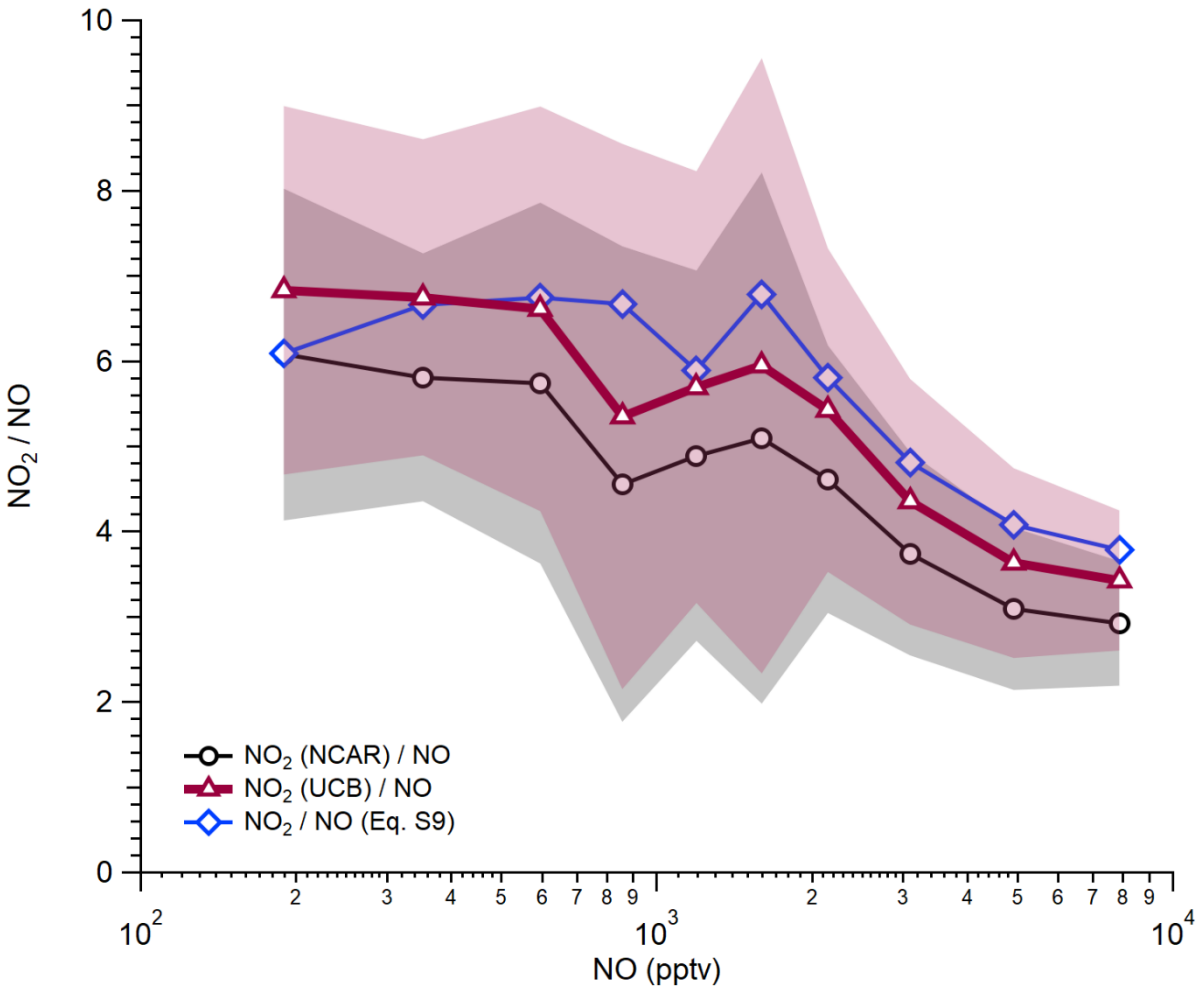

Figure S3. Binned NO_2-to-NO ratio, where NO is from NCAR chemiluminescence and NO_2 is either from NO_2 chemiluminescence (black) or University of California, Berkeley, laser induced fluorescence (dark red), versus NO. Shading is ±1σ spread in the observations for both observed ratios. The NO_2-to-NO ratio in blue is calculated using observations (Table 2) and Eq. S9.

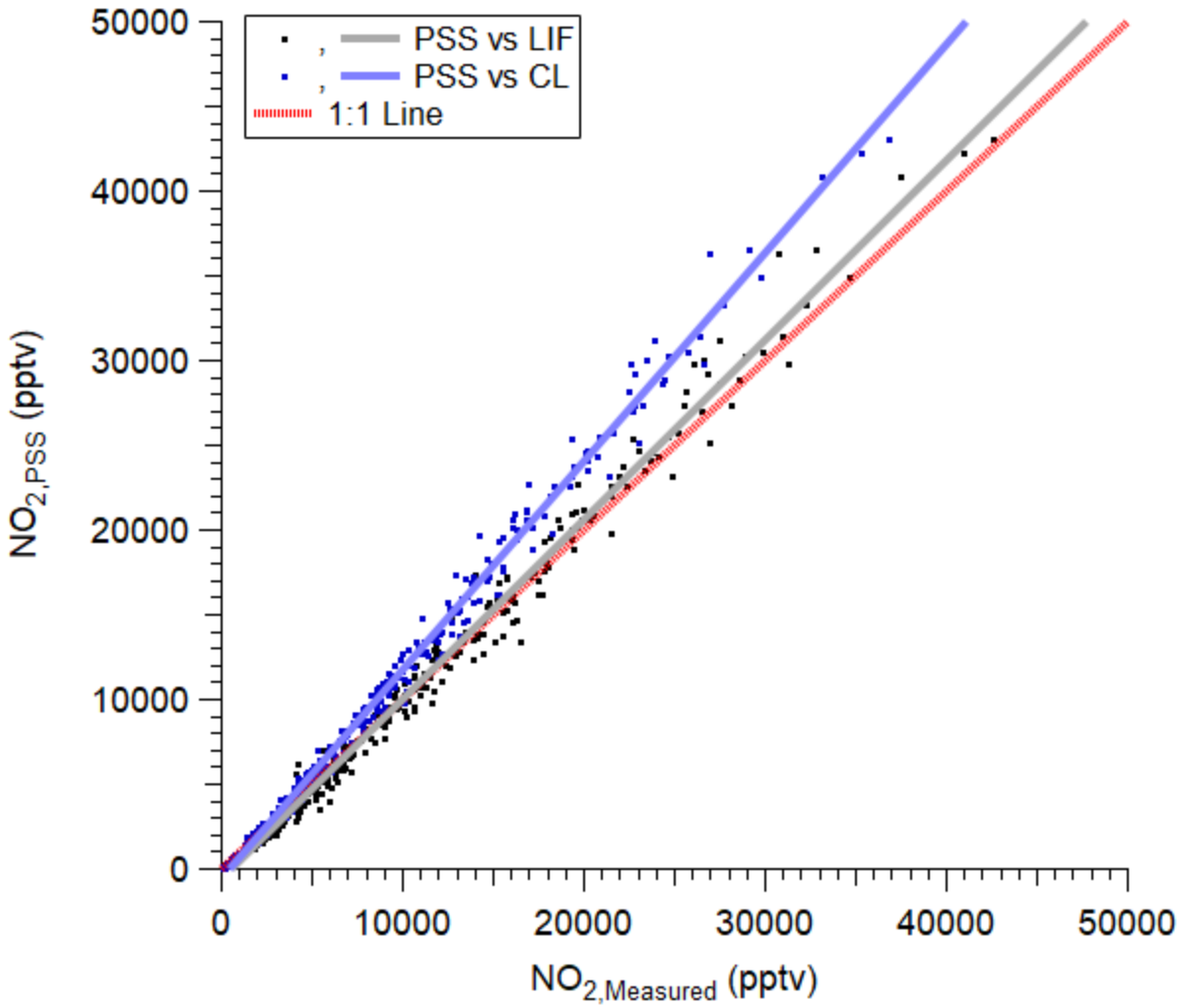

Figure S4. Scatter plot of predicted NO_2 PSS, from Eq. S9, and measured NO_2, from laser induced fluorescence (LIF) or chemiluminescence (CL). The PSS vs CL slope is 1.23, the PSS vs LIF slope is 1.06, and the 1:1 line is red.

S3. Error Analysis in Calculation of α_{eff} and R(VOC)

In Sect. 3.3, Eq. 8 – 11 assumes that $L(O_x)$ and $L(\sum ANs)$ is negligible. However, $L(O_x)$ is approximately 25% of the $P(O_x)$ over SMA (e.g., Figure 6). An analysis of how much unmeasured R(VOC) and the α_{eff} is impacted by neglecting these two terms is calculated using Eq. S9.

$$\frac{\Delta O_x}{\Delta \Sigma ANs} \approx \frac{P_{O_x}}{P\Sigma ANs} = \frac{\gamma(1-\alpha)R(VOC)[OH] - L(O_x)}{\alpha R(VOC)[OH] - L(\sum ANs)} \quad \text{(Eq. S9)}$$

Here, γ is the effective O_x produced per VOC reacted (1.53), α is the effective branching ratio to form $\sum$ANs, R(VOC) is the VOC and CO reactivity, and L_{Ox} and $L_{\sum ANs}$ are the loss terms for O_x and $\sum$ANs.

One limit in these equations is if $L(\sum ANs)$ is near 0 and $L(O_x)$ is important. At this limit, assuming all R(VOC) is captured by observations, this would lead to an α_{eff} of ~0.02. This is equivalent to the calculated α_{eff} using the observed VOCs and calculated secondary VOCs from F0AM and would indicate no missing R(VOCs).

However, there are multiple reasons to assume this limit in that $L(\sum ANs)$ is 0 is incorrect and that the observations do not capture α_{eff} and R(VOC). First, the total OH reactivity measured by Penn State indicates missing reactivity at low NO_x mixing ratios, as discussed in Sect. 3.3 and shown in Fig. 4. Second, the comparison of speciated and measured $\sum$PNs as well as the comparison of the F0AM calculated and measured $\sum$PNs indicates missing R(VOC) to account for the unmeasured PNs, as discussed in Sect. 3.1 and 3.4 and Fig. 2 and 5. Finally, González-Sánchez et al. (2023) showed that even for long-lived ANs, the lifetime is ~50 hours. However, for multifunctional ANs, this lifetime drops down to 2 – 16 hours. Note, however these multifunctional ANs are mainly from biogenic VOCs and not anthropogenic VOCs. Yet, as predicted in MCM (Jenkin et al., 2015), ANs from anthropogenic VOCs are expected to have similar lifetimes as ANs from biogenic VOCs.

To investigate the role of L(∑ANs) and L(O_x) on unmeasured R(VOC) and α, Eq. S9 instead of Eq. 11 is used. The results are summarized in Figure S4. If the ANs lifetime of 16 hours is assumed, which may be a lower limit, the average unmeasured R(VOC) decreases from $1.7^{+1.1}_{-0.4}$ s^{-1} to 1.4 s^{-1}, and the unmeasured α would be 0.09, leading to an α_{eff} of 0.032. Note, both of these values are very close to the values calculated assuming losses were negligible. For the unmeasured R(VOC) and α shown in Fig. 4, the ∑ANs lifetime would be equivalent to 11.5 hrs. This is in the range of lifetime for multifunctional ANs, but a lower limit (González-Sánchez et al., 2023). If the typical ANs lifetime shown in González-Sánchez et al. (2023), ~6 hrs, is assumed, the average unmeasured RVOC increases from $1.7^{+1.1}_{-0.4}$ s^{-1} to 2.2 s^{-1}. This would lead to an α_{eff} of 0.045. Note this is still with the uncertainty of R(VOC) found with the Penn State observations at low NO_x. Thus, though uncertainty in both ∑ANs lifetime and the unmeasured α impact the calculated unmeasured RVOC, (a) inclusion of the loss terms of both O_x and ∑ANs lies within the spread in observed RVOC at low NO_x mixing ratios and the associated calculated RVOC assuming the loss terms were negligible, (b) if the L(O_x) term is considered, the L(∑ANs) term must also be included as it is non-negligible in environments with freshly-produced, multifunctional ANs.

There are two potential other sources of uncertainty in the calculated, unmeasured RVOC—(1) assumed α for the F0AM secondary species and (2) α for aromatics. First, for α ranging from 0.00 – 0.10 for F0AM species, the unmeasured RVOC falls within the spread of observations and calculated unmeasured RVOC assuming F0AM α is 0.05. Thus, the calculated unmeasured is insensitive to the F0AM α until the F0AM α is greater than 0.10. Though the α values for secondary, oxygenated species is unconstrained (Orlando and Tyndall, 2012), α being greater than 0.10 is currently unexpected with what is currently known about chemistry of these secondary species. Second, the α for aromatic compounds was changed from the values found in

MCM (Jenkin et al., 2015) and Perring et al. (2013) to all being 0.01. This is due to recent a recent study finding that α is potentially lower for aromatic compounds (Xu et al., 2020). Even with this low α value for the aromatics, the average unmeasured RVOC is not greatly impacted, increasing from 1.7 to 1.8 s^{-1}. This is due to the aromatics accounting for a small fraction of the total α and ∑ANs.

Thus, though there are numerous assumptions and sources of uncertainty associated with constraining the unmeasured RVOC with the observations, the overall results of, on average, 1.7 s^{-1} unmeasured RVOC is robust. As these various sensitivity investigations minimally impact the calculated unmeasured RVOCs using the assumptions in the main text, the unmeasured RVOCs associated with $\alpha = 0.10$ and assuming the loss terms are negligible are used.

As described in Sect. S1 and Eq. 1 (and S7), HO_2 is important in the next O_x production. However, an intercomparison of measured and F0AM modeled HO_2 shows that the two values diverge from the one-to-one line at high NO_x mixing ratios (Figure S6a), where the measured HO_2 is higher compared to F0AM modeled HO_2. As this is at high NO_x mixing ratios, this impacts the calculated $P(O_x)$, where the measured HO_2 would suggest high $P(O_x)$ with increasing NO_x, whereas F0AM HO_2 shows decreasing $P(O_x)$ with increasing NO_x (Figures S6b). The latter, decreasing $P(O_x)$ with increasing NO_x, more closely aligns with theory (e.g., Sect. S1 and (Seinfeld. and Pandis, 2006)). Further, the latter more closely aligns with observations in that $P(O_x)$ increases with decreasing NO_x, e.g., the "NO_x penalty" (Jhun et al., 2015; Pusede and Cohen, 2012). Though calculations using observed HO_2 have suggested that $P(O_x)$ either remains constant and/or decreases wit the decreasing NO_x (e.g., Whalley et al., 2018, 2021), this does not align with both theory and the "NO_x penalty" observed, suggesting potential uncertainties for HO_2 at low

184 HO_2 and high NO_x mixing ratios. Thus, to be consistent with theory and "NO_x penalty"
185 observations, F0AM calculated HO_2 is used throughout the study.

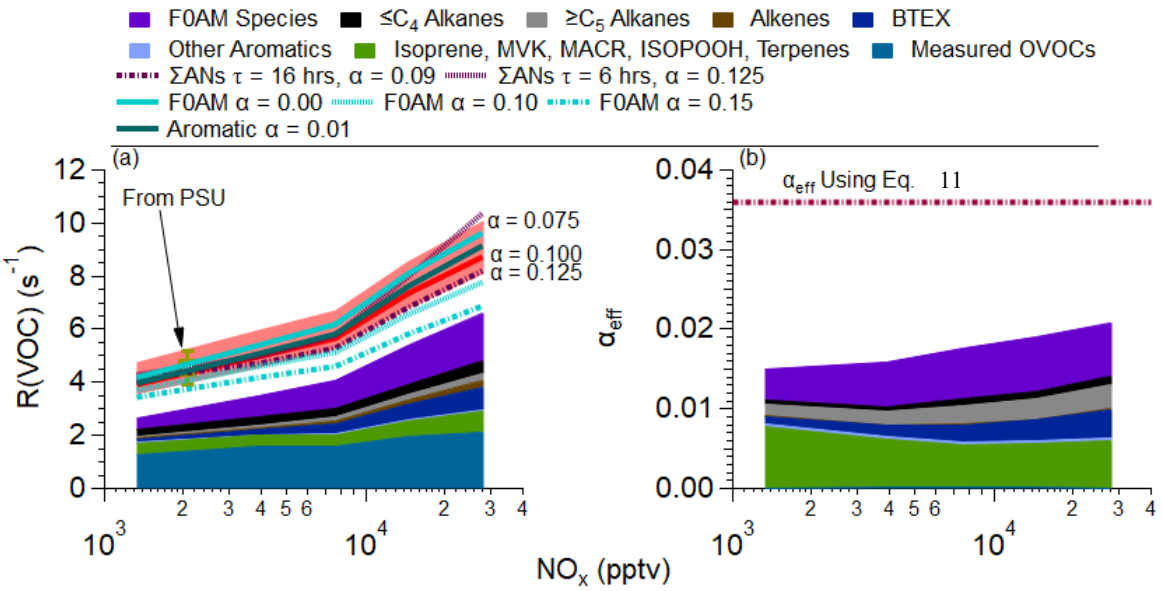

186

187 **Figure S5.** Same as Figure 4, but with the sensitivities discussed in Sect. S3, including inclusion
188 of O_x and ANs loss terms, range of α for F0AM secondary species, and lowering the aromatic α
189 value.

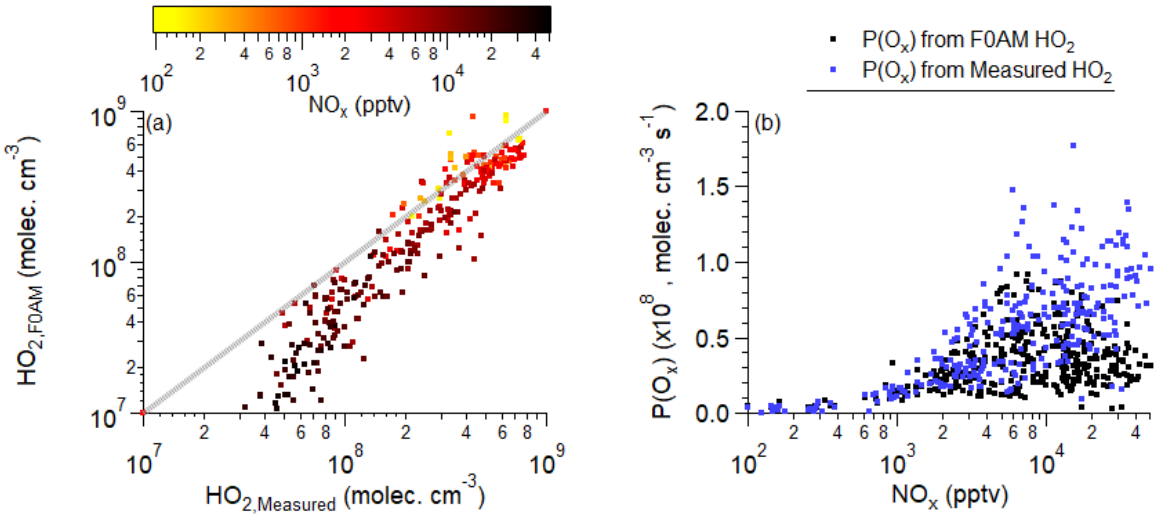

Figure S6. (a) Scatter plot of HO_2 predicted from F0AM vs measured HO_2, colored by measured NO_x mixing ratios. One-to-one line represented by the grey line. (b) Calculated $P(O_x)$, using Eq. 1, for HO_2 predicted by F0AM (black) or HO_2 measured (blue).

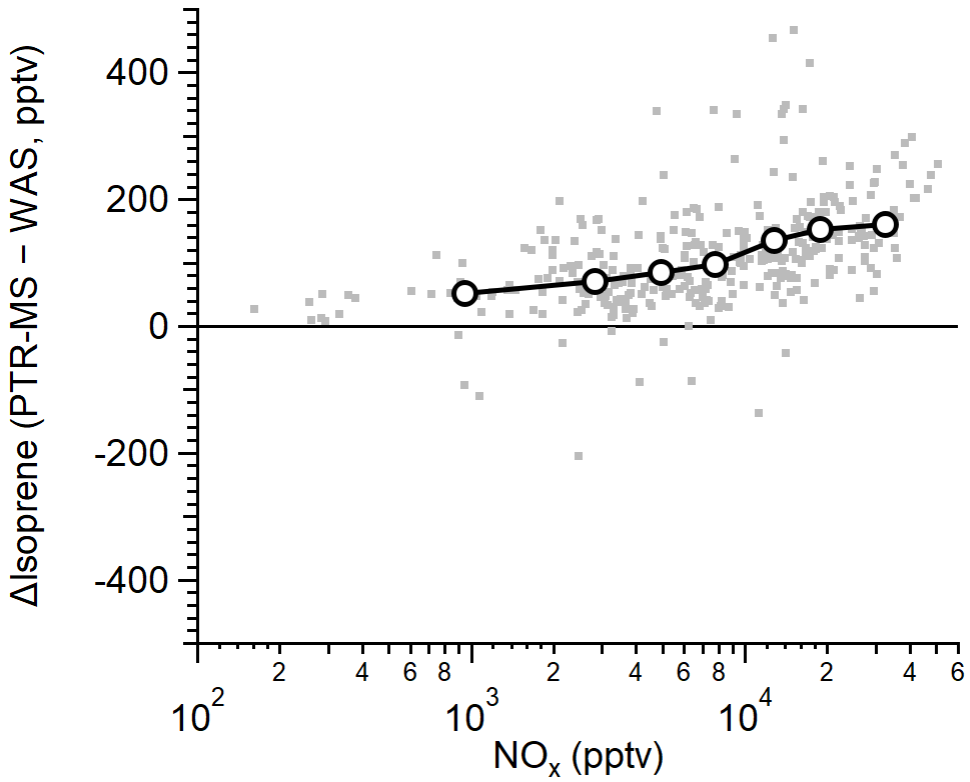

194

195 **Figure S7.** The difference in the isoprene mixing ratio measured by University of Oslo PTR-MS
196 and University of California, Irvine WAS, versus the observed NO_x. All data are shown in grey
197 and equally sized bins are shown in black for observations collected over the SMA.

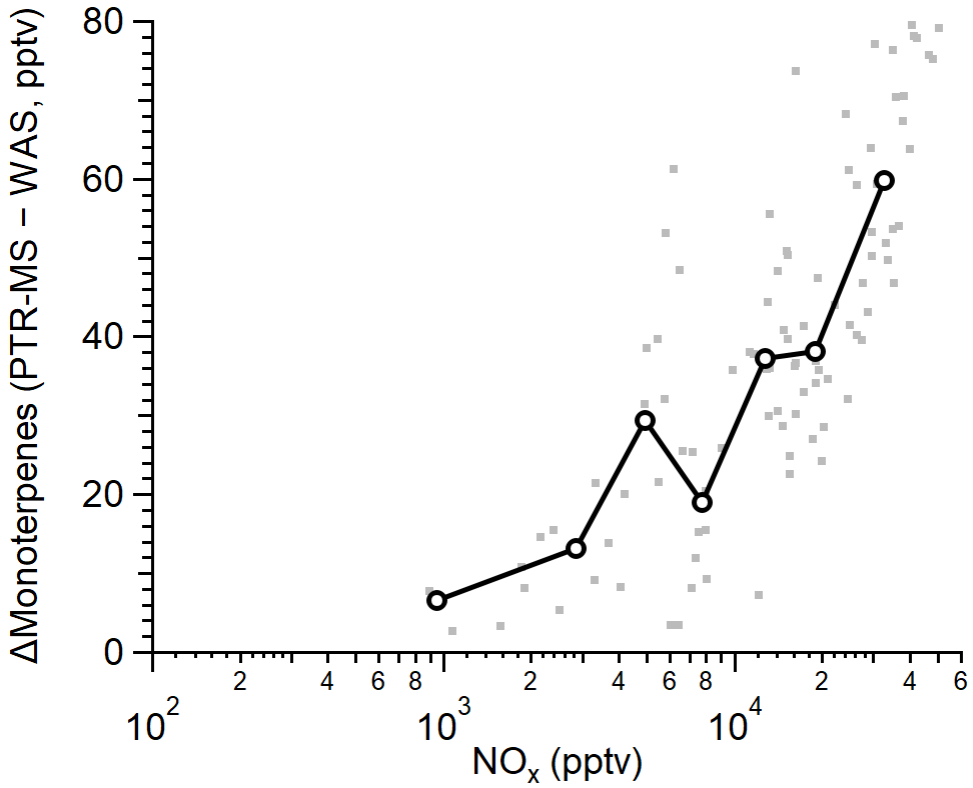

Figure S8. Same as Figure S7, but for monoterpenes. Lower amount of data is associated with the measurements being below detection limit for WAS.

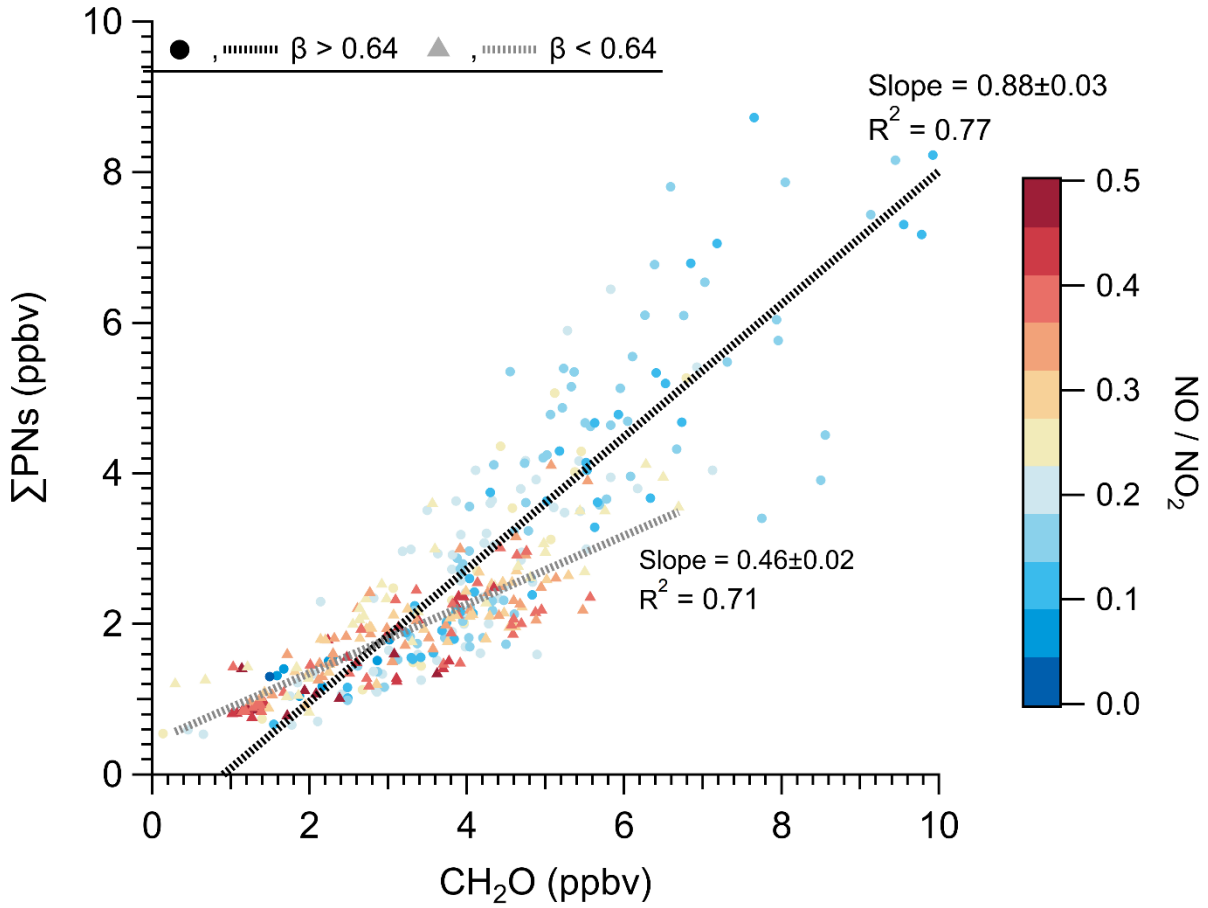

201

202 **Figure S9.** Same as Figure 3b, but with the data colored by the NO-to-NO_2 ratio. Further, the fits
203 are differentiated between the β value, where β value describes the fraction of time an acyl peroxy
204 radical ($R(O)O_2$) reacts with NO_2 versus NO. The β is equal to $(k_{R(O)O2+NO2}[NO_2])/($
205 $k_{R(O)O2+NO2}[NO_2]+k_{R(O)O2+NO}[NO])$.

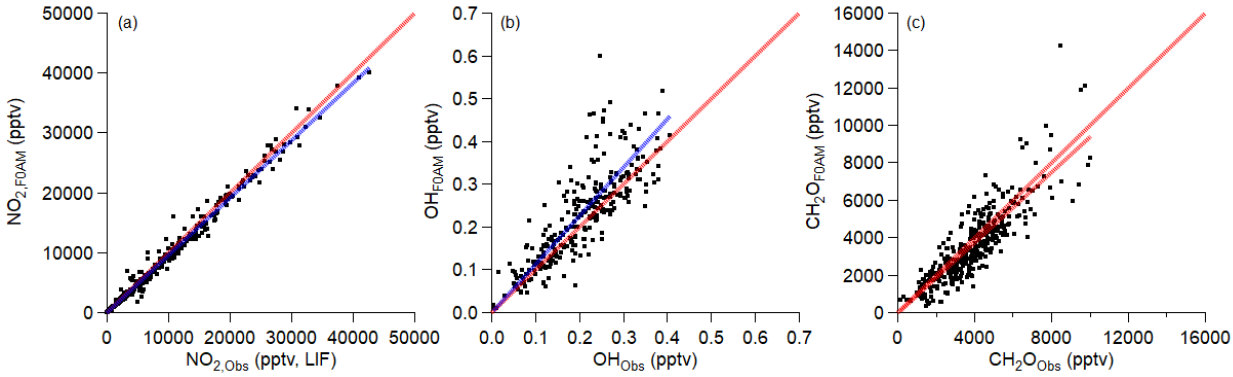

206

207 **Figure S10.** Evaluation of the F0AM model performance versus gases measured on DC-8 over
208 the SMA and not used to constrain the model. (a) Scatter plot of F0AM predicted NO_2 versus
209 observed NO_2 from UC Berkeley. (b) Scatter plot of F0AM predicted OH versus Penn State
210 observed OH. (c) Scatter plot of F0AM predicted CH_2O versus CAMS observed CH_2O.

S4. Sensitivity in F0AM Results with Missing R(VOC)

We add to the model a test of whether the estimated additional OH reactivity of ~1.7 s^{-1} would degrade model performance in simulating formaldehyde or OH. We add approximately 800 pptv of C_4H_9CHO (pentanal), on average, as a proxy for unmeasured aldehydes, such as octanal, nonanal, decanal, etc. The concentration of pentanal varies according to the calculated missing OH reactivity. The average OH reactivity from this species is ~0.5 s^{-1}. Total OH reactivity goes up by 1.2 s^{-1} after including all the products produced from the oxidation of pentanal. Therefore, the added primary species (pentanal) results in over twice as much reactivity from secondary oxidation products. The largest secondary oxidation products are smaller aldehydes (HOC_3H_6CHO, HOC_2H_4CHO, C_3H_7CHO), which have OH reactivity of 0.1 to 0.2 s^{-1} each. With the inclusion of ~0.5 s^{-1} pentanal to F0AM as a surrogate for missing R(VOC), OH is reduced by ~25% compared to the base model (Figure S9). We attribute this OH reduction to the build-up of the peroxynitrate ($C_5H_9NO_5$) from pentanal to approximately 500 pptv. This pentanal peroxynitrate is likely overestimated given the rapid exposure of PN species to warmer temperatures through mixing, as discussed by Crawford et al. (2021). Model formaldehyde change with the inclusion of ~0.5 s^{-1} pentanal to F0AM by < 5% (Figure S10). This is attributed to the balance of increased production of formaldehyde and RO_2 to convert NO to NO_2 by pentanal, but the decreased OH which then reduces production/conversion.

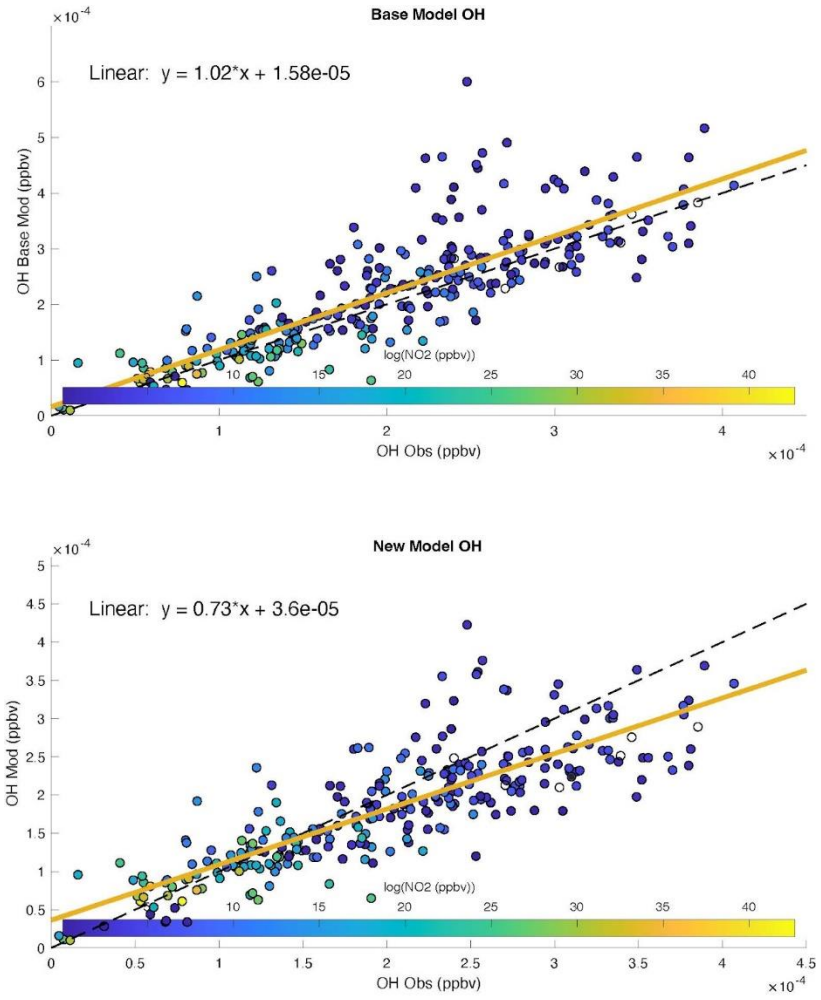

230

231 **Figure S11.** Comparison of F0AM predicted OH versus observed OH for the base F0AM model

232 (top) and sensitivity F0AM model that included ~0.5 s^{-1} pentanal to account for missing R(VOC).

233 The values are colored by observed NO_2 (note, the scale is in logarithmic scale).

234

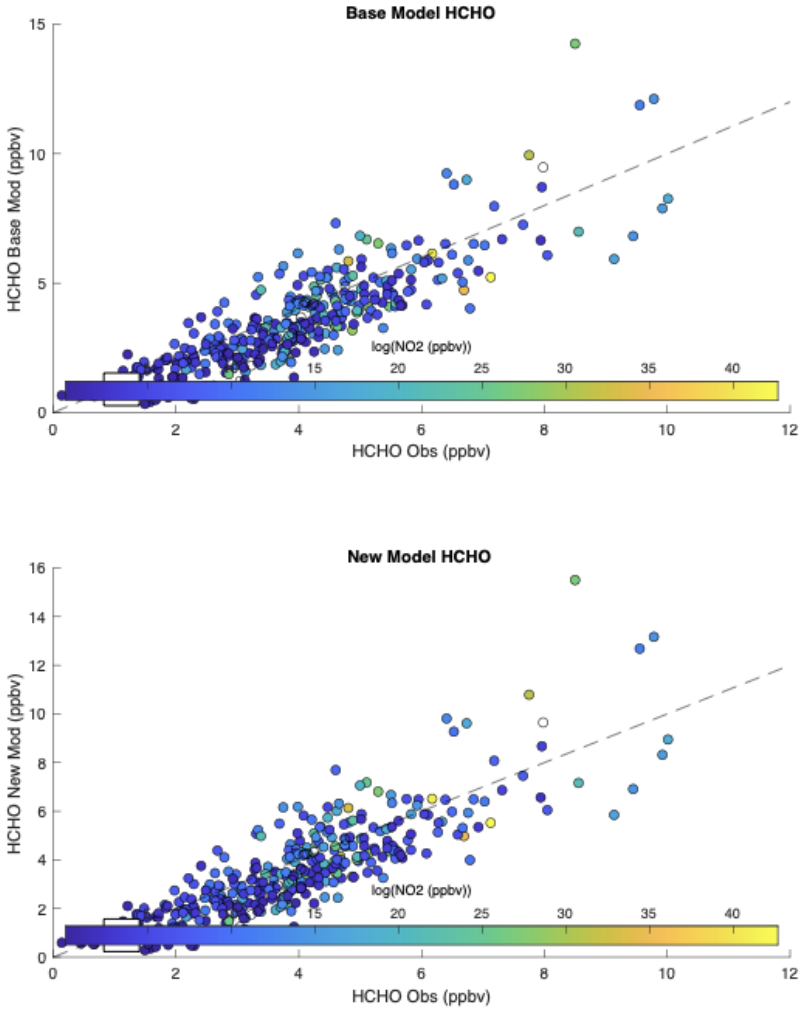

235

236 **Figure S12.** Same as Figure S11, except for formaldehyde.

237

S5. Aerosol Contamination of the CAFS Downwelling Optic

During KORUS-AQ ambient aerosols deposits were regularly evident on all leading edges of the aircraft, particularly during low altitude spirals near Seoul. The deposits collected on the leading edge of the downwelling CAFS optic (Figure S12), resulting in optical reductions in the actinic flux of up to 20%. The precise reductions depended on the aerosol coating efficiency and cleaning by precipitation. The optic was centered above the DC-8 fuselage in the zenith 1 port, just aft of the forward cabin exit door. The upwelling optic was unaffected, likely due to the larger aircraft boundary layer near its location under the aft fuselage.

Extensive analysis was required to correct the downwelling data. This involved identification of contaminated periods, characterization of the angular impact, optical thickness and time evolution. Corrections were applied to the direct beam only. Corrections to diffuse light were estimated to be small (<3%) and the corrective skill insufficient for application to the data. Such aerosol coating had not been detected during numerous high aerosol encounters on previous campaigns. They appear to result from unprecedented aerosol combinations in the SMA.

The final CAFS dataset includes a flagging scheme (Table S3) to tag the contaminated periods. For any quality flag > 0 the photolysis frequency uncertainties should be increased by 20% to account for the low bias during contamination. For quality flag 0 the uncertainty should be conservatively increased by 10% due to the uncertainty in the aerosol cleaning efficiency during the remainder of the flights.

Table S3. CAFS data quality flag summary

Quality Flag	Aerosol deposit Contamination?	Direct Beam Impacted?	Correction Applied?	Correction Source
0	No	No	No	-
1	Yes	No	No	-
2	Yes	Yes	Yes	Current spiral
3	Yes	Yes	Yes	Nearest spiral and turns
4	Yes	Unknown	No	Insufficient spiral data

Figure S13. Strong aerosol contamination of the optic following the flight on 19 May, 2016.

S6. Comparison in Calculating $P(O_x)$

Two different equations to calculate $P(O_x)$ are introduced in the main text – Eq. 1 and Eq. 9. Eq. 1 is more explicit as it is tracking the number of O_x molecules formed from all reactions of RO_2 and HO_2 molecules with NO (and accounting for the fraction of reactions where RO_2 and NO form ANs); whereas, Eq. 9 is simplified version and takes the reactivity averaged α and γ for the environment and fold HO_2 into the R(VOC). Comparing the $P(O_x)$ from the two equations is shown in Figure S13. Since Eq. 1 is more explicit, it is approximately 24% higher than Eq. 9, as Eq. 9 does not directly account for RO_2 concentrations and assumes the total amount of HO_2 molecules formed. Eq. 1 is more accurate as it is not assuming the total amount of HO_2 formed and thus used when directly calculating $P(O_x)$ (e.g., Fig. 6). Eq. 9 thus may lead to an under-estimation in unmeasured R(VOC); however, due to the number of unknowns and uncertainties, it cannot be evaluated at this time.

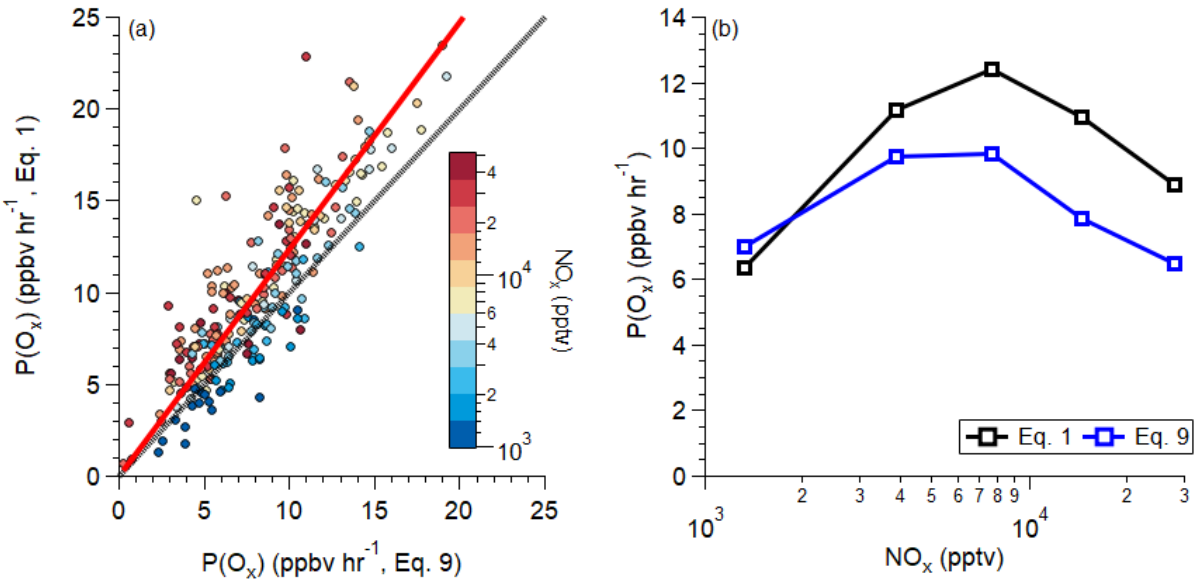

Figure S13. (a) Scatter plot of Eq. 1 versus Eq. 9 $P(O_x)$, colored by NO_x mixing ratios. The slope, 1.24, is red, and the 1:1 line is black. (b) Binned $P(O_x)$ for Eq. 1 (black) and Eq. 9 (blue).

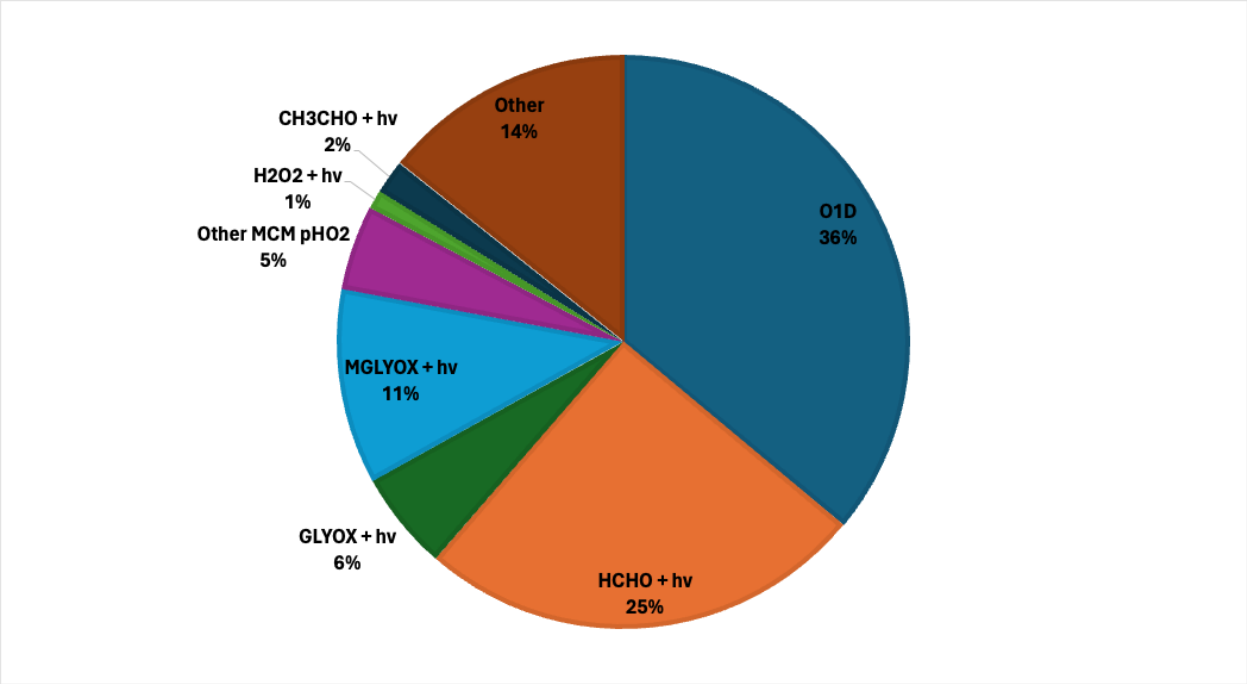

Figure S14. Fractional contribution for different sources of HO_x predicted from F0AM.

References

Crawford, J. H., Ahn, J. Y., Al-Saadi, J., Chang, L., Emmons, L. K., Kim, J., Lee, G., Park, J. H., Park, R. J., Woo, J. H., Song, C. K., Hong, J. H., Hong, Y. D., Lefer, B. L., Lee, M., Lee, T., Kim, S., Min, K. E., Yum, S. S., Shin, H. J., Kim, Y. W., Choi, J. S., Park, J. S., Szykman, J. J., Long, R. W., Jordan, C. E., Simpson, I. J., Fried, A., Dibb, J. E., Cho, S. Y., and Kim, Y. P.: The Korea-United States air quality (KORUS-AQ) field study, Elementa, 9, 1–27, https://doi.org/10.1525/elementa.2020.00163, 2021.

Farmer, D. K., Perring, A. E., Wooldridge, P. J., Blake, D. R., Baker, A., Meinardi, S., Huey, L. G., Tanner, D., Vargas, O., and Cohen, R. C.: Impact of organic nitrates on urban ozone production, Atmos Chem Phys, 11, 4085–4094, https://doi.org/10.5194/acp-11-4085-2011, 2011.

González-Sánchez, J. M., Brun, N., Wu, J., Ravier, S., and Clément, J.: On the importance of multiphase photolysis of organic nitrates on their global atmospheric removal, Atmos Chem Phys, 23, 5851–5866, https://doi.org/10.5194/acp-23-5851-2023, 2023.

Jenkin, M. E., Young, J. C., and Rickard, A. R.: The MCM v3.3.1 degradation scheme for isoprene, Atmos Chem Phys, 15, 11433–11459, https://doi.org/10.5194/acp-15-11433-2015, 2015.

Jhun, I., Coull, B. A., Zanobetti, A., and Koutrakis, P.: The impact of nitrogen oxides concentration decreases on ozone trends in the USA, Air Qual Atmos Health, 8, 283–292, https://doi.org/10.1007/s11869-014-0279-2, 2015.

Min, K.-E., Washenfelder, R. a., Dubé, W. P., Langford, a. O., Edwards, P. M., Zarzana, K. J., Stutz, J., Lu, K., Rohrer, F., Zhang, Y., and Brown, S. S.: A broadband cavity enhanced absorption spectrometer for aircraft measurements of glyoxal, methylglyoxal, nitrous acid, nitrogen dioxide, and water vapor, Atmos Meas Tech, 9, 423–440, https://doi.org/10.5194/amt-9-423-2016, 2016.

Orlando, J. J. and Tyndall, G. S.: Laboratory studies of organic peroxy radical chemistry: an overview with emphasis on recent issues of atmospheric significance, Chem Soc Rev, 41, 6294–6317, https://doi.org/10.1039/c2cs35166h, 2012.

Perring, A. E., Pusede, S. E., and Cohen, R. C.: An observational perspective on the atmospheric impacts of alkyl and multifunctional nitrates on ozone and secondary organic aerosol., Chem Rev, 113, 5848–70, https://doi.org/10.1021/cr300520x, 2013.

Pusede, S. E. and Cohen, R. C.: On the observed response of ozone to NOx and VOC reactivity reductions in San Joaquin Valley California 1995–present, Atmos Chem Phys, 12, 8323–8339, https://doi.org/10.5194/acp-12-8323-2012, 2012.

Sander, S. P., Abbatt, J. P. D., Barker, J. R., Burkholder, J. B., Friedl, R. R., Golden, D. M., Huie, R. E., Kolb, C. E., Kurylo, M. J., Moortgat, G. K., Orkin, V. L., and Wine, P. H.: Chemical Kinetics and Photochemical Data for Use in Atmospheric Studies, Evaluation No. 17, JPL Publication 10-6, Jet Propulsion Laboratory, Pasadena, 2011.

Schroeder, J. R., Crawford, J. H., Ahn, J. Y., Chang, L., Fried, A., Walega, J., Weinheimer, A., Montzka, D. D., Hall, S. R., Ullmann, K., Wisthaler, A., Mikoviny, T., Chen, G., Blake, D. R., Blake, N. J., Hughes, S. C., Meinardi, S., Diskin, G., Digangi, J. P., Choi, Y., Pusede, S. E., Huey, G. L., Tanner, D. J., Kim, M., and Wennberg, P.: Observation-based modeling of ozone chemistry in the Seoul metropolitan area during the Korea-United States Air Quality Study (KORUS-AQ), Elementa, 8, https://doi.org/10.1525/elementa.400, 2020.

Seinfeld., J. H. and Pandis, S. N.: Atmospheric Chemistry and Physics: From Air Pollution to Climate Change, Second., John Wiley & Sons, Inc., Hoboken, NJ USA, 1232 pp., 2006.

Thornton, J. A., Wooldridge, P. J., and Cohen, R. C.: Atmospheric NO_2: In-situ laser-induced fluorescence detection at parts per trillion mixing ratios, Anal Chem, 72, 528–539, https://doi.org/doi:10.1021/ac9908905, 2000.

Weinheimer, A. J., Walega, J. G., Ridley, B. A., Gary, B. L., Blake, D. R., Blake, N. J., Rowland, F. S., Sachse, G. W., Anderson, B. E., and Collins, J. E.: Meridional distributions of NO_x , NO_y , and other species in the lower stratosphere and upper troposphere during AASE II, Geophys Res Lett, 21, 2583–2586, https://doi.org/10.1029/94GL01897, 1994.

Whalley, L. K., Stone, D., Dunmore, R., Hamilton, J., Hopkins, J. R., Lee, J. D., Lewis, A. C., Williams, P., Kleffmann, J., Laufs, S., and Woodward-massey, R.: Understanding in situ ozone production in the summertime through radical observations and modelling studies during the Clean air for London project (ClearfLo), Atmos Chem Phys, 18, 2547–2571, https://doi.org/10.5194/acp-18-2547-2018, 2018.

Whalley, L. K., Slater, E. J., Woodward-massey, R., Ye, C., Lee, J. D., Squires, F., Mehra, A., Worrall, S. D., Bacak, A., Bannan, T. J., Coe, H., and Percival, C. J.: Evaluating the sensitivity of radical chemistry and ozone formation to ambient VOCs and NO_x in Beijing, Atmos Chem Phys, 21, 2125–2147, https://doi.org/10.5194/acp-21-2125-2021, 2021.

Xu, L., Møller, K. H., Crounse, J. D., Kjaergaard, H. G., and Wennberg, P. O.: New insights into the radical chemistry and product distribution in the OH-initiated oxidation of benzene, Environ Sci Technol, 54, 13467–13477, https://doi.org/10.1021/acs.est.0c04780, 2020.